**Correspondence to:**
V. F. Andrioli,
vania.andrioli@inpe.br;
vaniafatima@gmail.com

# Strong temperature gradients and vertical wind shear on MLT region associated to instability source at 23°S

V. F. Andrioli[1,2] (iD), P. P. Batista[2] (iD), Jiyao Xu[1] (iD), Guotao Yang[1] (iD), Wang Chi[1], and Liu Zhengkuan[1] (iD)

[1]National Space Science Center, Chinese Academy of Sciences, Beijing, China, [2]Instituto Nacional de Pesquisas Espaciais, São José dos Campos, Brazil

**Abstract** Na lidar temperature measurements were taken successfully from 2007 to 2009 in the mesopause region over São José dos Campos (23.1°S, 45.9°W). Strong gradients on these vertical temperature profiles are often observed. A simple theoretical study has shown that temperature gradient of at least $-8$ K/km is required concurrently with the typical tidal wind shear in order to generate dynamical instability in the MLT region. We have studied vertical shear in horizontal wind related to atmospheric tides, inferred by meteor radar, with the aim of analyzing instability occurrence. These wind measurements were taken from an all-sky meteor radar at Cachoeira Paulista (22.7°S, 45°W). Two years of simultaneous data, wind and temperature, were used in this analysis which represent 79 days, totalizing 589 h of simultaneous observations. We realize that the condition for the local Richardson number ($Ri$) dropping below the critical value of instability ($Ri < 0.25$) is often reached in 98% of the analyzed cases. The mean probabilities for occurrence of convective and dynamical instabilities, in the altitude region between 82 and 98 km, were observed to be about 3% and 17.5%, respectively. Additionally, vertical distribution of these probabilities has revealed a weak occurrence of dynamical instability around 90 km, and this fact can be related to the double mesopause typically observed in this site.

## 1. Introduction

It is widely accepted that atmospheric waves transport their energy and momentum from the lower to the upper atmosphere. Also, scientific community recognizes that most of these waves, mainly gravity waves (GWs), break and deposit energy and momentum in the mesosphere/lower thermosphere (MLT) region. This process causes the turbulence increasing, which in combination with the temperature inversion in mesopause region makes the MLT as one of the most interesting regions for investigation in atmospheric physics. These vertical gradients on temperature profiles can be greater than the dry adiabatic lapse rate leading to convective instability occurrence. Likewise, in the presence of vertical shear in horizontal wind, dynamical instabilities can also occur. Numerous theoretical and numerical simulation studies have helped to improve our understanding of the role of these instabilities in the GW breaking [e.g., *Hodges*, 1967; *Lindzen*, 1981; *Fritts and Rastogi*, 1985; *Fritts and Yuan*, 1989; *Andreassen et al.*, 1994, 1998; *Fritts et al.*, 1994, 1997, 1998; *Isler et al.*, 1994; *Lombard and Riley*, 1996; *Sonmor and Klaassen*, 1997; *LeLong and Dunkerton*, 1998a, 1998b; *Liu et al.*, 1999]. Also, some observational studies have shown the presence of these instabilities and related them to the breaking of GW (see *Fritts and Alexander* [2003, and references therein] for a complete discussion of instabilities role on GW propagation) leading to the conclusion that both of these instabilities are dominant mechanisms for GW breaking in the MLT region.

Owing to the importance of these instabilities in the mesopause, their characterization is fundamental for our improvement in the understanding of the dynamics in this region. Up to now such studies have been done only in the Northern Hemisphere [e.g., *Zhao et al.*, 2003; *Li et al.*, 2005a, 2005b; *Sherman and She*, 2006]. Although these four works presented annual variation on the relative frequency of occurrence in convective and dynamical instabilities, they diverge with respect to the value of these probabilities. For example, the mean probability for convective instability occurrence ranges from less than 1.4% to 8% [*Sherman and She*, 2006; *Zhao et al.*, 2003]. This indicates that more studies are necessary for a better comprehension of instabilities and how they vary from one site to another. Also, since all the reported works were done in Northern Hemisphere and there is no report of such work in the Southern Hemisphere where different background atmospheric condition exists, it acts as motivation for the present paper.
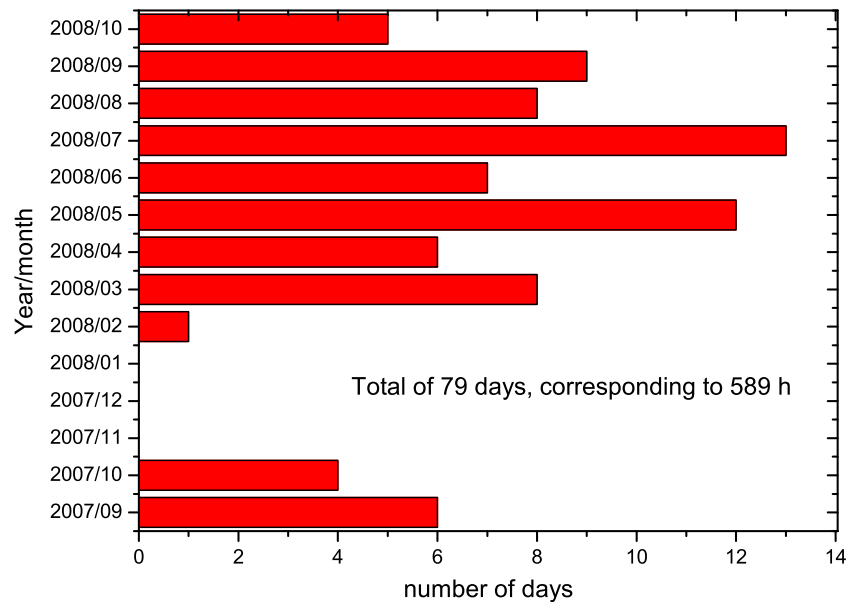
**Figure 1.** Histogram showing the simultaneous Na lidar temperature and meteor Wind data between 2007 and 2008.

We have analyzed 2 years of simultaneous Na lidar temperature and meteor radar wind data and found that the condition for the local unstable region (based on Richardson number, $Ri < 0.25$) is often reached in about 98% of the analyzed cases. Moreover, in some of these cases the Brunt-Väisälä frequency reaches values about 4 times smaller than the standard ones (~5 min), implying the existence of strong vertical temperature gradients. Additionally, large vertical shear in horizontal wind are also often observed which contribute for the high frequency of instability occurrence.

In this work, we investigate the dynamic and convective instabilities in the MLT region by using temperature and wind data simultaneously. The occurrence of these instabilities can be a start to a favorable feedback for wave breaking, momentum deposition, and acceleration of the mean flow, and also on the large vertical wind shear [*Liu et al.*, 2014].

In section 2 we present some theoretical tests investigating the importance of temperature gradient and horizontal wind gradient for the $Ri$ reaching the critical values for the dynamical instability. In section 3, we show some results and comparison between dynamical and convective instabilities. On section 4 we present the comments and discussion, and finally, on section 5, we present a summary.

## 2. Method

Sodium temperature lidar is located at São José dos Campos (23°S, 46°W), and an all-sky meteor radar is located at Cachoeira Paulista (22.7°S, 45°W), about 100 km away. Our Na lidar operated measuring temperature profiles between 2007 and 2009. Transmitter generates 589 nm pulses by mixing the output of two pulsed neodymium:yttrium/aluminum/garnet (Nd:YAG) lasers, seeded by continuous wave Nd:YAG seeders operating at 1064 and 1319 nm, respectively. By thermally tuning the seeders it is possible to switch the output wavelength between the sodium D2a resonance peak and the crossover minimum. Temperature is determined by comparing the scattering from the sodium layer at these two wavelengths, and it allows determining temperature with 300 m range resolution and about 3 min time resolution. More details about the lidar system and the method for inferring temperature can be found at *She et al.* [1990], *Yang et al.* [2010], and *Clemesha et al.* [2011].

Hourly winds from 80 to 100 km, with 2 km height resolution, were inferred by an all-sky meteor radar. Details about the meteor radar wind approach and technical information about the used system can be found at *Hocking et al.* [2001] and *Batista et al.* [2004], respectively. According to these previous studies, error on meteor wind analysis is about 1 m/s (86–93 km) and increase to around 2 or 3 m/s

on the top (above 95 km) and the bottom (bellow 84 km) of meteor region. This meteor radar has been operating almost uninterruptedly since April 1999. But, there are two long periods in which radar stopped working: from August 2006 to September 2007, and from November 2008 to June 2012. The simultaneous data from September 2007 to October 2008 totalize 89 nights. Out of which only 79 nights that have more than 3 h of temperature observations (totalize 589 h) have been analyzed in this study. Monthly variation of the number of our simultaneous data observation is shown in Figure 1. Clearly, the period with more observation is from May to July of 2008. On the other hand, there is no observation during November and December 2007 and January 2008. It is because in summer period cloudiness and rains occur almost every evening in this region, making it impossible for Na lidar operation.

Richardson's number was used as a dynamical instability indicator. It is a nondimensional index that measures the fluid's tendency to remain stratified. When $Ri$ drops down to 0.25 the flow starts to be turbulent. So a necessary condition but not sufficient condition for instability is $Ri$ less than 0.25 [*Miles*, 1961]. It can be calculated by

$$R_i = \frac{N^2}{\left(du/dz\right)^2} \tag{1}$$

$$\text{with } N^2 = \left(\frac{g\left(\partial T/\partial z - \alpha^*\right)}{T(z)}\right) \tag{2}$$

where $du/dz = \frac{\sqrt{(\Delta U^2 + \Delta V^2)}}{\Delta z}$ is the vertical shear in horizontal wind, $z$ is height, $\partial T/\partial z$ is the vertical gradient of temperature, $g$ is the gravity acceleration, and $\alpha^* = -9.5$ (K/km) is the dry adiabatic lapse rate. Equation (2) is the square of Brunt-Väisälä frequency ($N^2$), and convective instability may occur when $N^2$ is negative. It is also important to mention that several authors have suggested that instabilities may occur outside of these critical limits [e.g., *Fritts and Alexander*, 2003, and references therein]. Nevertheless, several observational studies in the mesopause region have shown good agreement with these indicators [*Hecht et al.*, 1997; *Williams et al.*, 2002; *Li et al.*, 2005a; *Cai et al.*, 2014; *Takahashi et al.*, 2014]. Hence, in the present work, we will use $N^2 < 0$ and $0 < Ri < 0.25$ for convective and dynamical instabilities, respectively.

Brunt-Väisälä frequency depends basically on vertical temperature gradients; on the other hand, $Ri$ depends not only on temperature but also on the horizontal wind. So simultaneous measurements of temperature and winds are required for evaluating convective and dynamical instabilities. Most of the studies about instabilities in the MLT region were done by using a high-resolution Doppler lidar for measuring both temperature and winds [e.g., *Li et al.*, 2005a; *Sherman and She*, 2006]. Although we have a high temporal/spatial resolution in temperature measurements, our Na lidar cannot obtain winds. So we decided to use a meteor radar data for measuring horizontal winds in the MLT region. In order to minimize the temporal and spatial resolution differences between these two equipments, wind data were interpolated by a spline function in time. Moreover, temperature profiles were smoothed in width of 2 km vertical and 0.5 h in time. Owing to the fact that for convective instability analysis we need only temperature measurements, we have used the high temperature resolution. So $N^2$ were inferred into two different temporal/spatial resolutions to evaluate convective instability and its probability of occurrence; vertical temperature gradients were inferred over the smoothed temperature profiles and using the numerical differentiation using 3-point, Lagrangian interpolation, which provides $N^2$ values at the same resolutions as temperature. However, for dynamical instability we need $N^2$ at the same resolution as the winds. Therefore, we averaged those smoothed temperature profiles, each 2 km height and half hour, and the vertical temperature gradient were inferred by the declivity of a linear fitting every two subsequent vertical points. Comparison between the two different ways for inferring $N^2$, not shown here, has revealed similar results supporting the methodology. The vertical shear in horizontal wind was calculated by the vector sum of the vertical variability in each wind component: $\sqrt{(\Delta U^2 + \Delta V^2)}$, $\Delta U = U_{z2} - U_{z1}$, where $U_z$ is the mean the zonal wind at the altitude $z$ ($z2 > z1$), and so on for the meridional component, $\Delta V$.

**Table 1.** Values for the Parameters Used for Each One of the Three Tests

| Parameters | Test 1 | Test 2 | Test 3 |
|---|---|---|---|
| $U_M, V_M$ (m/s) | 10, 5 | 10, 5 | 10, 5 |
| $U_D, V_D$ (m/s) | 50, 60 | 50, 60 | 50, 60 |
| $\lambda_D$ (km) | 24 | 24 | 24 |
| $U_{SD}, V_{SD}$ (m/s) | 0, 0 | 20, 10 | 20, 10 |
| $\lambda_{SD}$ (km) | – | 80 | 80 |
| $N$ (min) | 5 | 5 | ? |
| $\Delta z$ (km) | 2 | 2 | 2 |

## 2.1. Test Study

In order to understand how the temperatures and the wind gradients can lead to a critical value of $Ri < 0.25$ we have performed simple theoretical studies by using MLT winds and $N$ frequency models representing commonly observed values. Horizontal winds were inferred considering only the prevailing winds plus the two more important tidal components by using the following equations:

$$U(z,t) = U_M + U_D \sin\left(2\pi\left(\frac{t}{T_D} - \frac{z}{\lambda_D}\right)\right) + U_{SD}\sin\left(2\pi\left(\frac{t}{T_{SD}} - \frac{z}{\lambda_{SD}}\right)\right) \tag{3}$$

$$V(z,t) = V_M - V_D \cos\left(2\pi\left(\frac{t}{T_D} - \frac{z}{\lambda_D}\right)\right) - V_{SD}\cos\left(2\pi\left(\frac{t}{T_{SD}} - \frac{z}{\lambda_{SD}}\right)\right) \tag{4}$$

where $U$ and $V$ are zonal and meridional components of the horizontal wind, respectively; $T$ is the wave period; the $\lambda$ is the vertical wavelength; $t$ is time; and $z$ represents the corresponding altitude. The subscript indices, $M$, $D$, and SD, represent mean wind, diurnal tide, and semidiurnal tide, respectively.

We have implemented three tests as displayed in Table 1. The values attributed to each parameter were based on earlier observational studies made at the same location by *Batista et al.* [2004]. On test 1 we have considered the background wind with diurnal tide amplitude and short vertical wavelength observed on equinoctial condition. The purpose of this test is to study if wind shear from diurnal tide alone can generate dynamical instability. So we consider that Brunt-Väisälä period does not change either with time or with height, assuming the value of 5 min. The parameter $\Delta z$ was defined by the vertical wind height resolution, and for this reason, its value is set as 2 km. From Figure 2 we can see that even if the shear is large, about 30 m/s/km, the $Ri$ values are around 2. Hence, far from the value of 0.25 required for the onset of dynamical instability. Therefore, even in the equinoctial time when diurnal tide has large amplitude and shear, its shear rate alone cannot exceed the fluid's tendency to remain stratified. In the second test, we include the semidiurnal tide, and so the shears became a bit larger than in the test 1. Again, no changes on the Brunt-Väisälä period were considered. In Figure 3 we can see the results for $Ri$ become smaller than those from test 1, but never reaching 0.25. In test 3, we estimate the buoyancy frequency boundary considering equinoctial tide conditions in order to satisfy $Ri = 0.25$. In Figure 4 we can see that on the regions of larger wind gradients, $N \sim 13$ min is enough for starting the instability. Note from equation (2), that $N^2$ depends on the vertical gradient of temperature. Considering equinoctial tidal wind pattern, a temperature gradient of at least $-8$ K/km is required for starting the dynamical instability. A quick search on temperature data during fall, March/April,
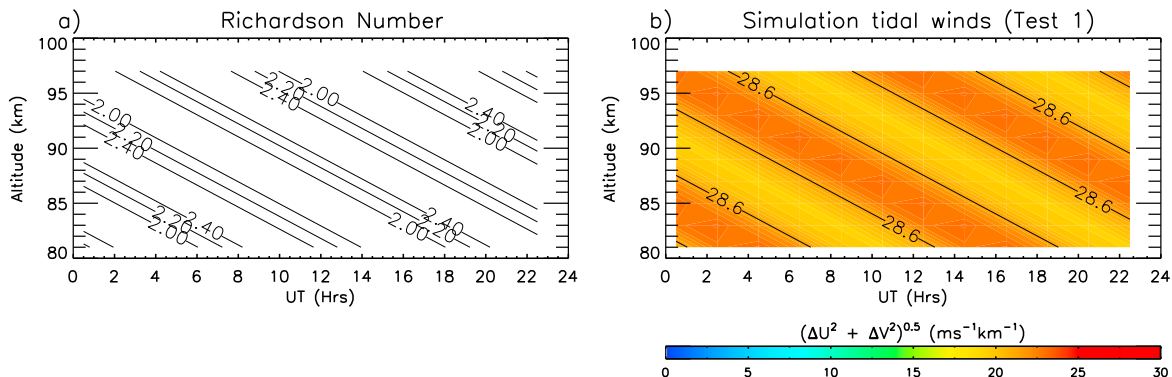


**Figure 2.** (a) Richardson number expected for test 1, considering Brunt-Väisälä frequency constant, and (b) vertical shear in horizontal wind due to only diurnal tide, commonly observed at equinoctial time.
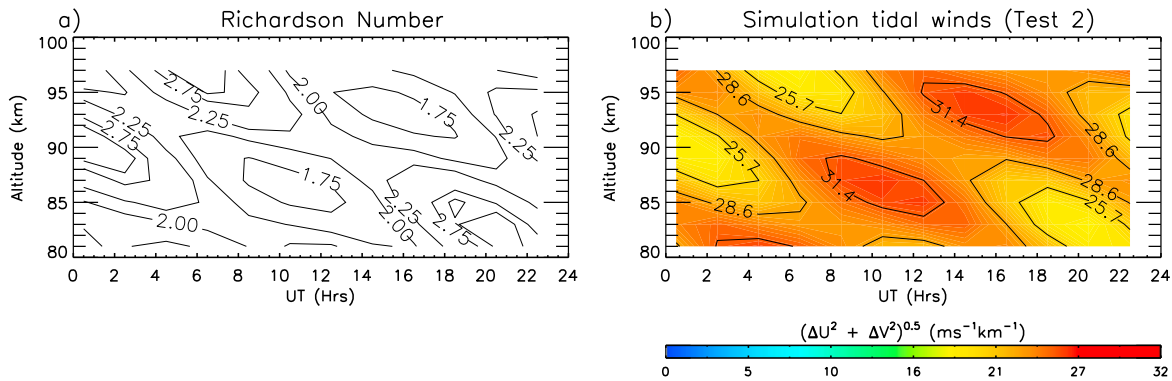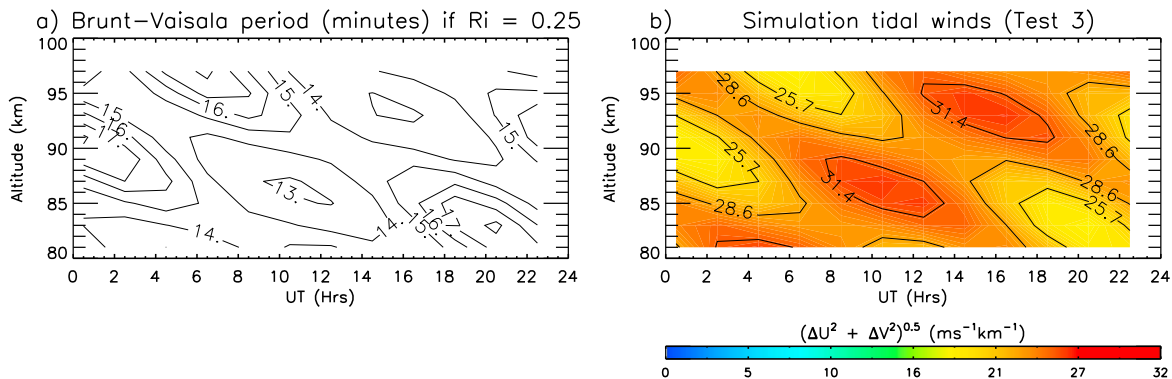
**Figure 3.** (a) Richardson number expected for test 2 and (b) horizontal wind gradient due to diurnal and semidiurnal tidal wind conditions commonly observed at equinoctial time.

and spring, September/October, totalizing 33 nights with more than 3 h observation shows that this condition is often reached. In order to exemplify, we show in Figure 5 measured temperature contour plot for the night of 5 and 6 September 2008 as a function of time and height, with no smoothing. We clearly see the downward movement of the local temperature minimum, suggesting the presence of tidal propagation, from around 95 km at 22:00 UT to about 87 km at 26:00 UT. On the right side of the same figure it shows the time averaged temperature profile where a vertical gradient of temperature of $\sim -9$ K/km between 83 and 89 km can clearly be seen. This suggests that at some moments and regions there are temperature gradients even stronger than that, as shown in Figure 6 (middle). So we decide to infer $Ri$ and $N^2$ on all simultaneous data with more than 3 h observation and study the seasonality of the probability of dynamical and convective instabilities to occur. These probabilities are determined by the relative frequency of occurrence of each instability. For example, the probability for convective instability: $P(N^2 < 0) =$ (total number of events with $N^2 < 0$)/(total observation) $\times 100\%$.

## 3. Results

Figure 6 shows the contour plot for temperature (Figure 6, top), vertical temperature gradient (Figure 6, middle), and square of Brunt-Väisälä frequency ($N^2$) (Figure 6, bottom) during 5 September 2008. In this case, we have used a numerical differentiation in order to get the vertical gradients. We can clearly see that the temperature gradients (Figure 6, middle) can reach values stronger than $-11$ K/km, around 87 km after 24:30 UT. Moreover, the dotted contour in Figure 6 (bottom) indicates the zero values for $N^2$. So we can observe that for the same regions where temperature gradients were stronger than $-9$ K/km the $N^2$ became negative, indicating a convective instability. To this specific night the probability of convective instability occurrence is around 4%. In order to compare convective and dynamical instabilities, zonal and meridional wind components are shown in Figures 7a and 7b, respectively. Moreover, to emphasize the tidal presence, we show 48 h



**Figure 4.** (a) Test simulation of Brunt-Väisälä period threshold expected if Richardson number is 0.25. (b) Horizontal wind gradient due to tidal wind conditions commonly observed at equinoctial time.
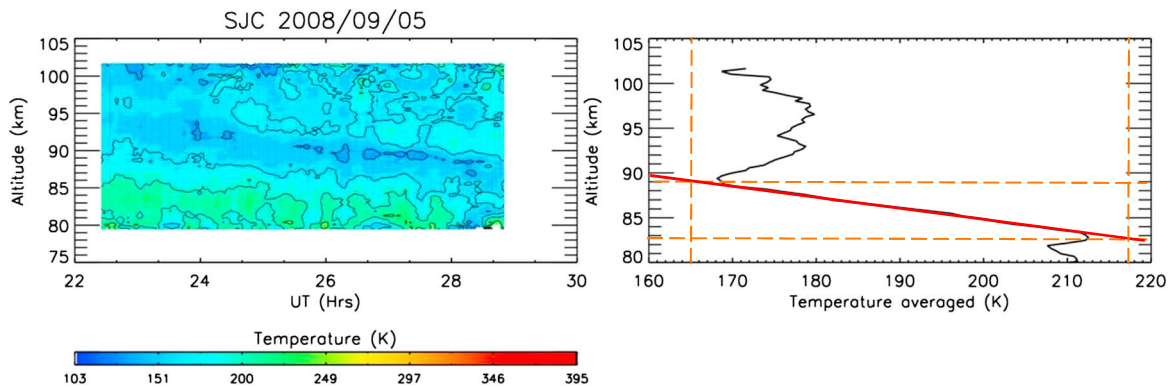
**Figure 5.** Temperature measured with Na lidar at São José dos Campos on 5 September 2008.

of meteor radar data, starting on 00:00 UT on 5 September 2008. We can see the well-defined diurnal tide propagation with its downward phase propagation, for example, in the zonal component, where positive phase starts on 00:00 UT around 100 km and reaches 80 km at around 24:00 UT. The dashed rectangle indicates the simultaneous times with temperature measurements. We can see that the zonal wind was not so large at that moment, but the meridional wind has its amplitude increasing, showing the phase quadrature movement of the tide. Inside of this rectangle we can see that vertical shear occurs in both components, being stronger at higher altitudes. This is confirmed in Figure 7c where vertical shear of horizontal wind is larger above 90 km. Still on the same figure, it shows the temperature gradient (Figure 7d); however, in this figure it was inferred by the angular coefficient from a linear fitting at each 2 km and 1 h interval. The altitude axis corresponds to the midpoint of height interval. Comparing to the previous figure, we can see that the results are very similar, so both techniques can be used to infer gradients. Supporting our thesis, the temperatures gradient reached $-11$ K/km around 24:30 UT and centered on 87 km. Moreover, we can see that gradients of at least $-4$ K/km are holding through almost all the observation period, from 85 to 88.5 km.

Richardson numbers were inferred for this event, and it can be observed in Figure 8a. For better identification
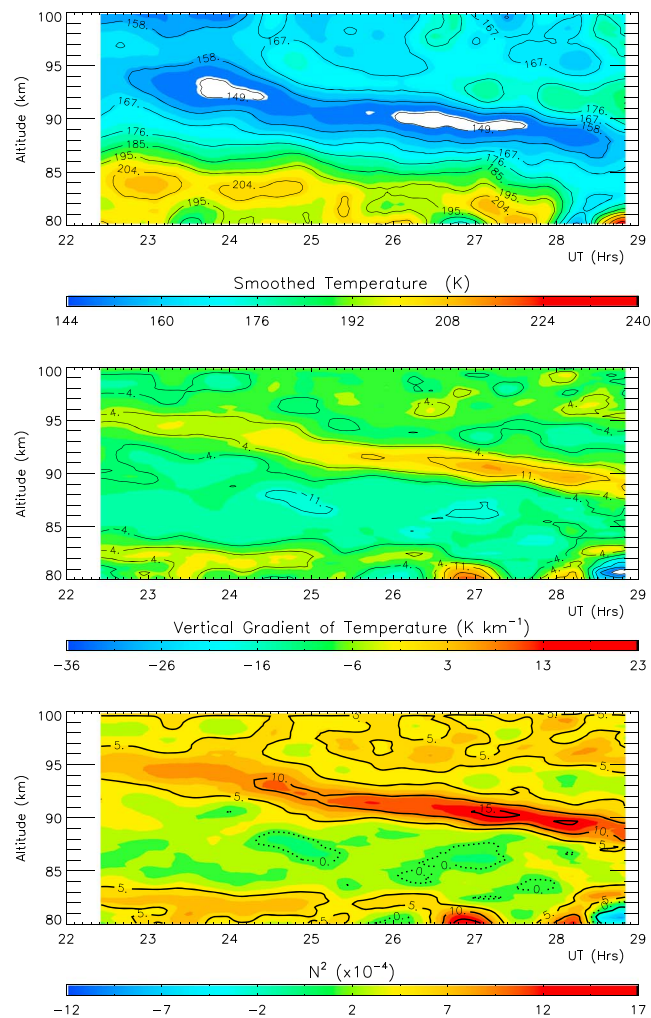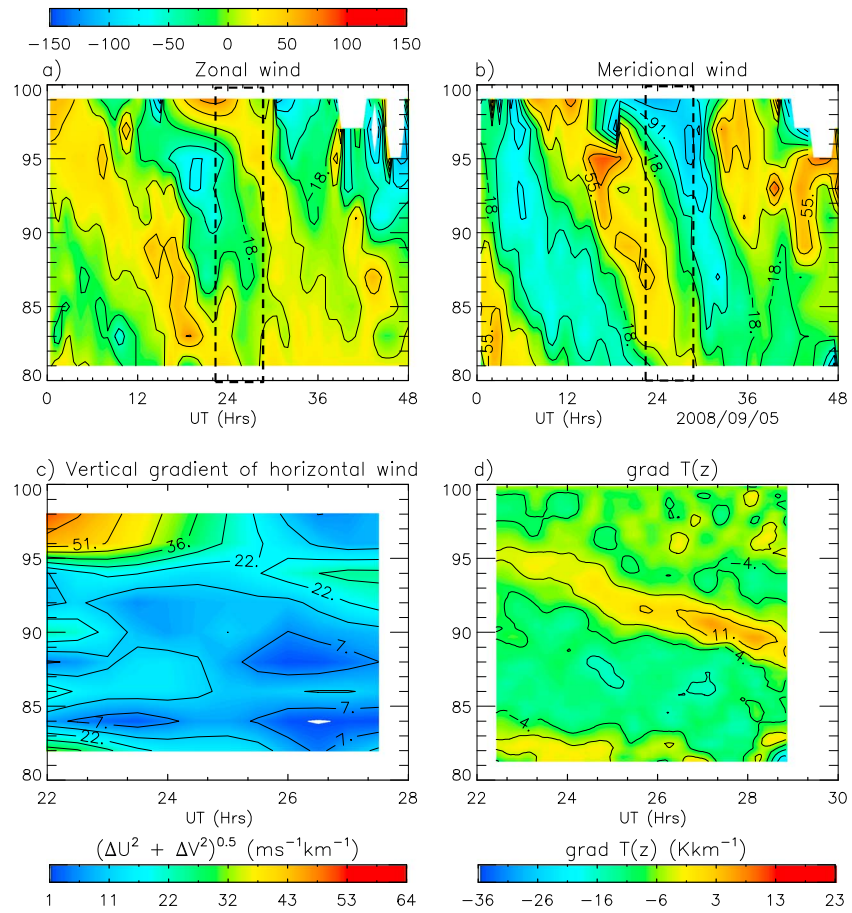


**Figure 6.** (top) Smoothed temperature, its (middle) vertical gradient, and the (bottom) square of Brunt-Väisälä frequency. The dotted lines on Figure 6 (bottom) identify the zero values, so inside of this contour $N^2 < 0$. All these results were obtained with a Na lidar temperature at São José dos Campos, on 5 September 2008.

**Figure 7.** Hourly (a) zonal and (b) meridional wind (m/s) data obtained with an all-sky meteor radar at Cachoeira Paulista, on 5 and 6 September 2008. (c) The vertical shear of horizontal wind at simultaneous time as the observation on temperature. (d) The vertical temperature gradient inferred by the angular coefficient from a linear fitting at each 2 km and 1 h interval.
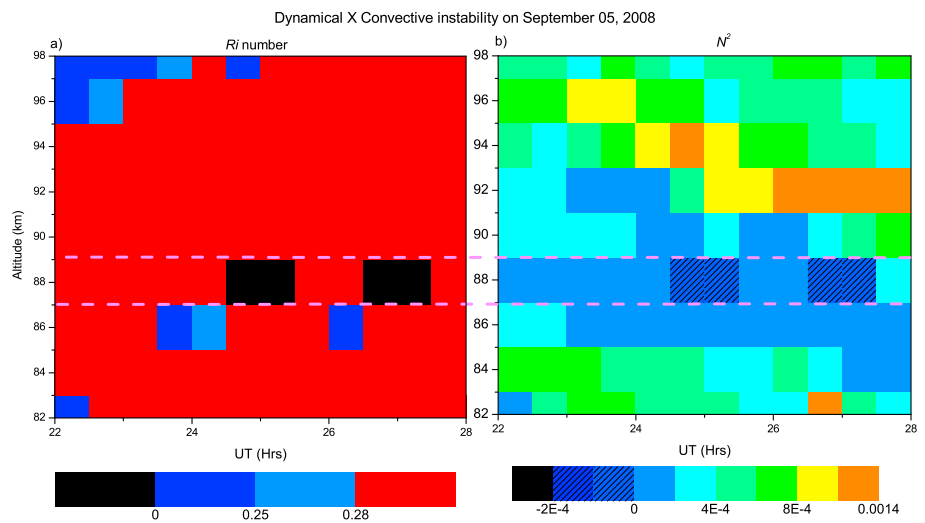


**Figure 8.** Comparison between dynamical and convective instabilities. (a) $Ri$ obtained with a Na lidar temperature at São José dos Campos and meteor radar wind data simultaneous observed on 5 September 2008. Values in dark blue indicate dynamical instability limits 0.25. (b) Brunt-Väisälä frequency, crosshatch, indicates negative values and an indicative of convective instability.
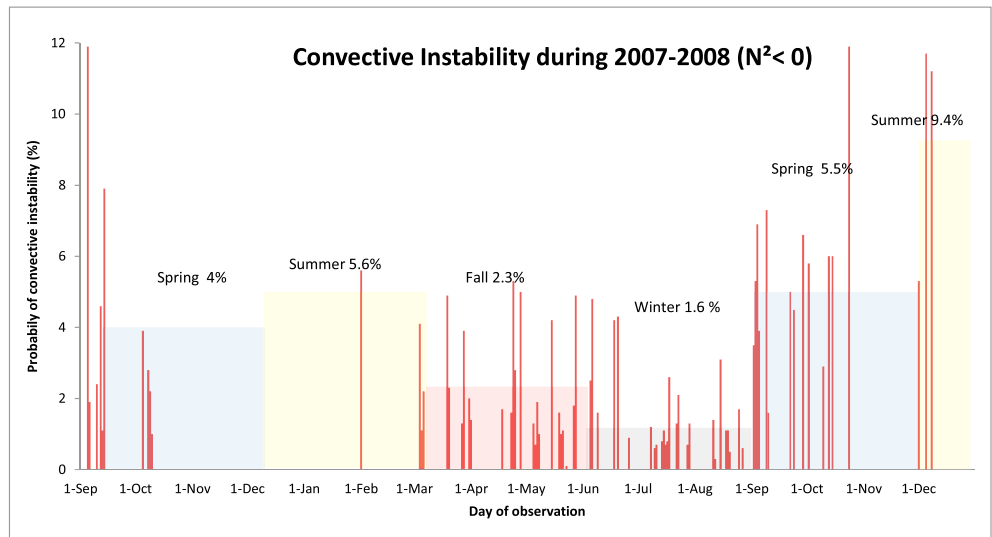
**Figure 9.** Statistical analysis of seasonal probability occurrence of convective instability, $N^2 < 0$. The color shades correspond to each season: the light blue represents spring, the yellow represents summer, the light red represents fall, and the light grey corresponds to the measurements during Winter.

of dynamical instability condition $0 < Ri < 0.25$, the black regions indicate $Ri < 0$; the blue region indicates $0 < Ri < 0.25$, and the light blue and red regions indicate no instability condition reached. On this day, we can observe that instability condition was reached at several regions; at the beginning of night on 22:30 UT it occurs in two regions around 82 km and above 95 km, in this last altitude, extending up to 23:30 UT. Also, at 23:30 UT, a possibility of dynamical instability is reached around 86 km, rising to 88 km around 24:30 UT and coming back at 26:30 UT up to 27:00 UT again at 86 km. Focusing on this last case, the dynamical instability occurrence between 85 and 87 km can be compared with convective instability, $N^2 < 0$, Figure 8b in the same figure. The dashed pink line indicates the altitude layer of the convective instabilities, from 87 to 89 km, and we can see that the dynamical instability happened below and before the convective one. This fact is also observed on the other cases analyzed. This happens as a consequence of equations (1) and (2), $Ri$ reduces its values as wind shear increases and/or $N^2$ becomes smaller. On the other hand, $N^2$
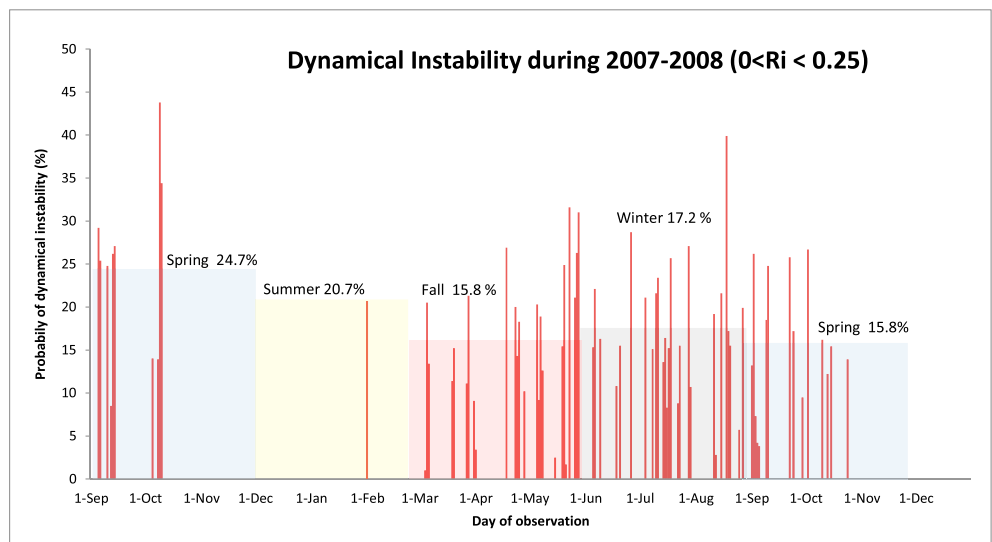


**Figure 10.** Statistical analysis of seasonal relative occurrence of the dynamical instability, $0 < Ri < 0.25$. The color shades correspond to each season: the light blue represents spring, the yellow represents summer, the light red represents fall, and the light grey corresponds to the measurements during winter.
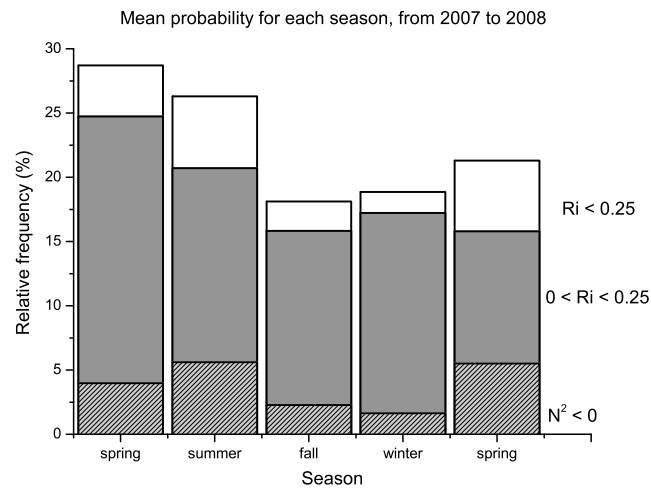
Mean probability for each season, from 2007 to 2008



**Figure 11.** Comparison of mean seasonal probability occurrences.

became negative only when temperature vertical gradient is smaller than the adiabatic lapse rate. That mean as altitude increases, the vertical temperature gradient is becoming more negative and the $N^2$ decreases its values allowing the condition for dynamical instability occurrence. Meanwhile, $N^2$ continues decreasing till it becomes negative and convective instability is reached. Moreover, as a consequence of equation (1), at the same time when convective instability happens, $Ri$ values became negative. This can be seen again at 26:30 UT. Also, the probability of occurrence of dynamical instability on 5 September 2008 is ~8%.

In order to evaluate the variation of occurrence of convective instability with the time of the year we present in Figure 9 the probability for all data analyzed. As $N^2$ values depend only of temperature measurements, we extended this analysis up to December 2008, so we can have a better sample for summer. We can observe an annual behavior when convective instability has a minimum probability of occurrence in winter and a maximum in summer, with large day to day variability, though. Moreover, the probability for convective instability remains below 6% most part of the year.

The seasonal variation of the relative frequency for the occurrence of dynamical instability is presented in Figure 10. On this statistical analysis, we can see that dynamical instability has a minimum probability of occurrence in fall 2008 and in spring 2008, and maxima during spring 2007 and winter 2008. Comparing to Figure 9, it is evident that the probability for dynamical instability is much higher than for convective instability. The ratio between probability of dynamic and convective instabilities is 5.6. The mean probabilities of convective and dynamical instabilities are observed to be ~3% and 17.5%, respectively. Additionally, both instabilities have an annual variation in the relative frequency of occurrence, although having their maximum in different seasons. These are more evident in Figure 11, where all mean probabilities are displayed together. So we can easily compare the seasonal variability of convective and dynamical instabilities. Note that we kept the mean probability for summer; however, this is not representative for this season owing the low sampling, only two nights as shown in Figure 1. Then, disregarding summer, a maximum is observed on spring for both dynamical and convective instabilities. Furthermore, a minimum probability of dynamical instability occurs either on fall as on the second spring. On the other hand, convective instability occurs with lower probability on winter. The mean probability of occurrence of any unstable region based on $Ri < 0.25$ remains higher than 17% at any season for both 2007 and 2008. Also, this total instability probability has an annual variation with maximum in spring and minimum in fall.

We also evaluate the height distribution of these probabilities as it can be seen in Figure 12. We can clearly see that the dynamical instability has almost the same pattern behavior of its height probability distribution among seasons. In other words, dynamical instability rarely occurs from 84 to 92 km through the year. Also, we can note the highest occurrence of dynamical instability above 95 km. For convective instability, on the other hand, it seems not to have a height preference for occurrence. It remains almost constant at all altitudes. However, convective instability presents much more season to season variability than dynamical ones.

## 4. Discussion

We have analyzed ~590 h of simultaneous temperature and wind data at the MLT region from 2007 to 2008 at around 23°S, in order to study dynamical and convective instabilities. Our analyses have shown that the condition for local unstable region (based on $Ri < 0.25$) from 82 to 98 km is often reached, about 98% of the analyzed cases, very close to the 90% observed by *Li et al.* [2005a]. Furthermore, the
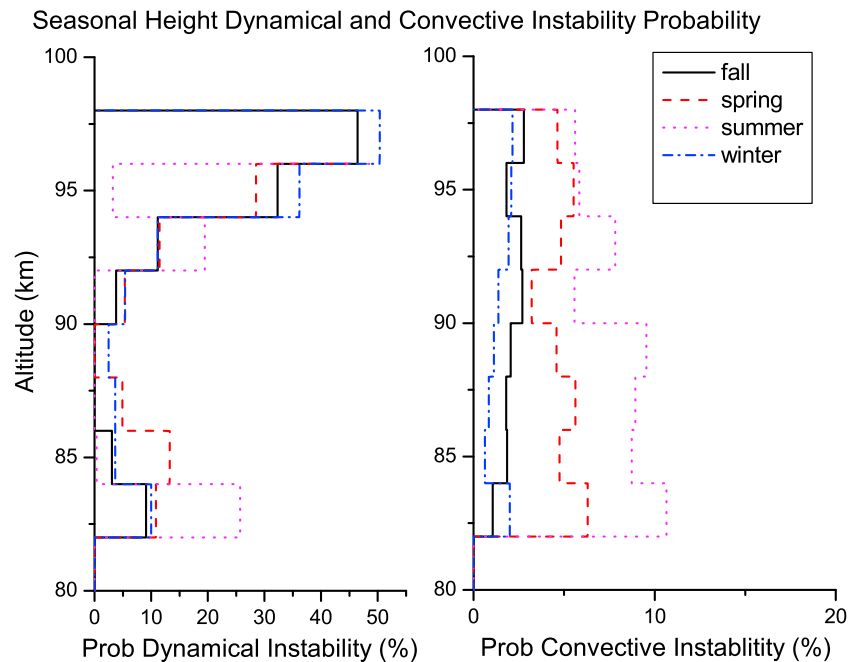
**Figure 12.** Vertical distribution of probabilities for each season. The full black line represents fall, the dashed red line indicates spring, the dotted pink means summer, and the dash-dotted blue line represents winter.

dynamical instability generally occurs below and before the convective instability in accordance with the previous works from *Zhao et al.* [2003] and *Li et al.* [2005a]. *Zhao et al.* [2003] using a high-resolution Na lidar wind and temperature data collected at Starfire Optical Range, near Albuquerque, NM (35.0°N, 106.5°W), attributed the found behavior to the phase difference between tidal temperature and wind perturbations. They also observed that both instabilities have a minimum probability of occurrence in summer and a maximum in winter, partially agreeing with our results at least with respect to an annual cycle. Moreover, they have shown that semidiurnal tides have significant impacts on the distribution of convectively unstable regions. This is because the convective instability depends basically on negative vertical gradient of temperature, so they found that the convective instability occurs generally in the upper part of semidiurnal tidal temperature perturbation.

*Li et al.* [2005a] reported the characteristics of instabilities in the mesopause region over Maui, HI (20.7°N, 156.3°W), using also a Na lidar measurements. They studied 19 nights, ~133 h of high-resolution wind and temperature data. Moreover, in their work they found that mean probabilities of convective and dynamical instabilities are observed to be 2.9% and 10%, respectively. Their probability for convective instability occurrence is very close to 3.1% found in the present work, which can be attributed to the fact that we are using almost the same resolution of temperature data, 3 min and 300 m, to evaluate $N^2$. So the wave spectra which could induce convective instability starting on $N$ period ~5 min, for both works, are the same. For dynamical probability, though, their relative frequency is much lower than the 17.5% we obtained. In this case, it is important to remember that we are using lower temporal (0.5 h) and height (2 km) resolution when inferring the vertical wind shear; therefore, one would expect fewer occurrences of dynamic instability since we had reduced the resolution of $N^2$ to that of the wind shear. *Sherman and She* [2006] also studied the dynamical and convective instabilities at mesopause region, over Fort Collins, CO (41.1°N, 105.1°W), using Na lidar temperature and wind data. They found that at a given altitude, the probability for convective instability is less than 1.4% for all seasons and the probability for dynamic instability (in the sense of Richardson number) ranges from 2.7% to 6.0%. They also investigated the influence of using lower resolution of data and the impact on the probabilities. They attributed their lower probability instabilities to time integration (15 min or 1 h) so short-period GWs were smoothed out. Moreover, they show large wind shear in higher altitudes, often exceeding 40 m/s/km near 100 km, which they attribute to the combination of high amplitudes of tides and long-period GW. The ratio of relative frequency of occurrence between dynamic and convective

instabilities from Fort Collins was 5.0 (using the same resolution for temperature and wind), close to the present analysis, 5.6. So this suggests that long-period GW (longer than 30 min) can be the responsible for the dynamical instability.

The lower probability of dynamical instability occurrence at around 90 km is also reported by *Li et al.* [2005a]; not being so pronounced as shown in Figure 12, though. The probability of dynamical instability drops to zero at around 87 km, for almost all seasons, indicating a stable region around this altitude through the year. *Clemesha et al.* [2011] reported that the average temperature profiles typically show double mesopause, a primary close to 100 km and a secondary close to 87 km; this is also reported by *Yu and She* [1995] and *Xu et al.* [2007]. This double mesopause implies a positive temperature vertical gradient around 90 km, and so a stable layer is established. Hence, the amplitude of the waves can keep growing and their breaking will occur at somewhat higher altitude. The more interesting thing is that this stable layer is well defined at all seasons, showing that this pattern remains throughout the year. This can be a result of a quite uniform altitude and temperature of the mesopause throughout the year at low latitude, as reported by *Xu et al.* [2007]. Moreover, double mesopause will also create a negative vertical temperature gradient, establishing the primary mesopause around 100 km, and so turning this region favorable for instabilities to occur. This agrees well with the increasing in the dynamical probability occurrence around 95 km shown in Figure 12. It is important to note that our analysis is done with temperature and wind data measured at night. Likewise, it is well known that both variables have time dependence, so these characteristics of dynamical and convective instabilities might change in 24 h observation. For this reason, more studies are necessary in order to clarify this possible time dependence on the instabilities characteristics as well as their implications in the MLT dynamics.

## 5. Summary

Our study has shown that dynamical and convective instabilities occur almost all nights, namely, 98% ($Ri < 0.25$). This is an indicative that the favorable condition for starting the processes of GW breaking is often happening. The mean probabilities of convective and dynamical instabilities to occur, at any altitude from 82 to 98 km, are observed to be ~3 and 17.5%, respectively. Our results agree in part with those presented by *Li et al.* [2005a], i.e., larger probability for dynamical instability than convective. Moreover, it is observed an annual seasonal variation in the probabilities of convective instability with minimum occurrence on winter. However, the seasonal variation on probability for dynamical instability seems to have a year-to-year dependence. The difference in resolution used to evaluate convective ($N^2 < 0$) and dynamical ($0 < Ri < 0.25$) instabilities and the higher relative frequency of occurrence for dynamical instability suggest that long-period gravity wave (period $> 30$ min) should be responsible for keeping the long duration of this instability. Distribution of instabilities as a function of altitude reveled an almost constant probability of convective instability; on the other hand, dynamical instability is rarely observed around 90 km, showing a stable layer around this altitude. This last is in good agreement with the double mesopause occurrence reported by *Clemesha et al.* [2011]. Still, more studies are necessary in order to clarify this seasonal dependence of convective instabilities and the impact of data resolution as well as their implications in the MLT dynamics.

## References

Andreassen, O., C. E. Wasberg, D. C. Fritts, and J. R. Isler (1994), Gravity wave breaking in two and three dimensions: 1. Model description and comparison of two-dimensional evolutions, *J. Geophys. Res.*, 99, 8095–8108, doi:10.1029/93JD03435.

Andreassen, O., P. O. Hvidsten, D. C. Fritts, and S. Arendt (1998), Vorticity dynamics in a breaking internal gravity wave. Part 1. Initial instability evolution, *J. Fluid Mech.*, 367, 27–46, doi:10.1017/S0022112098001645.

Batista, P. P., B. R. Clemesha, A. S. Tokumoto, and L. M. Lima (2004), Structure of the mean winds and tides in the meteor region over Cachoeira Paulista, Brazil (22.7°S,45°W) and its comparison with models, *J. Atmos. Sol. Terr. Phys.*, 66, 623–636, doi:10.1016/j.jastp.2004.01.014.

Cai, X., T. Yuan, Y. Zhao, P.-D. Pautet, M. J. Taylor, and W. R. Pendleton Jr. (2014), A coordinated investigation of the gravity wave breaking and the associated dynamical instability by a Na lidar and an Advanced Mesosphere Temperature Mapper over Logan, UT (41.7°N, 111.8°W), *J. Geophys. Res. Space Physics*, 119, 6852–6864, doi:10.1002/2014JA020131.

Clemesha, B., D. Simonich, and P. Batista (2011), Sodium lidar measurements of mesopause region temperatures at 23°S, *Adv. Space Res.*, 47, 1165–1171, doi:10.1016/JASR201011030.

Fritts, D. C., and L. Yuan (1989), Stability analysis of inertia-gravity wave structure in the middle atmosphere, *J. Atmos. Sci.*, 46, 1738–1745, doi:10.1175/1520-0469(1989)046<1738:SAOIWS>2.0.CO;2.

Fritts, D. C., and M. J. Alexander (2003), Gravity wave dynamics and effects in the middle atmosphere, *Rev. Geophys.*, 41(1), 1003, doi:10.1029/2001RG000106.

Fritts, D. C., and P. K. Rastogi (1985), Convective and dynamical instabilities due to gravity wave motions in the lower and middle atmosphere: Theory and observations, *Radio Sci.*, *20*, 1247–1277, doi:10.1029/RS020i006p01247.

Fritts, D. C., J. R. Isler, and O. Andreassen (1994), Gravity wave breaking in two and three dimensions: 2. Three dimensional evolution of instability structure, *J. Geophys. Res.*, *99*, 8109–8123, doi:10.1029/93JD03436.

Fritts, D. C., J. R. Isler, J. H. Hecht, R. L. Walterscheid, and O. Andreassen (1997), Wave breaking signatures in sodium densities and OH nightglow: 2. Simulation of wave and instability structures, *J. Geophys. Res.*, *102*, 6669–6684, doi:10.1029/96JD01902.

Fritts, D. C., S. Arndt, and O. Andreassen (1998), Vorticity dynamics in a breaking internal gravity wave. Part 2. Vortex interactions and transition to turbulence, *J. Fluid Mech.*, *367*, 47–65, doi:10.1017/S0022112098001633.

Hecht, J. H., R. L. Walterscheid, D. C. Fritts, J. R. Isler, D. C. Senft, C. S. Gardner, and S. J. Franke (1997), Wave breaking signatures in OH airglow and sodium densities and temperature: 1. Airglow imaging, Na lidar, and MF radar observations, *J. Geophys. Res.*, *102*, 6655–6668, doi:10.1029/96JD02619.

Hocking, W. K., B. Fuller, and B. Vandepeer (2001), Real-time determination of meteor-related parameters utilizing modern digital technology, *J. Atmos. Sol. Terr. Phys.*, *63*(2–3), 155–169, doi:10.1016/S1364-6826(00)00138-3.

Hodges, R. R., Jr. (1967), Generation of turbulence in the upper atmosphere by internal gravity waves, *J. Geophys. Res.*, *72*, 3455–3458, doi:10.1029/JZ072i013p03455.

Isler, J. R., D. C. Fritts, and O. Andreassen (1994), Gravity wave breaking in two and three dimensions: 3. Vortex breakdown and transition to isotropy, *J. Geophys. Res.*, *99*, 8125–8137, doi:10.1029/93JD03437.

LeLong, M.-P., and T. J. Dunkerton (1998a), Inertia-gravity wave breaking in three dimensions. 1. Convectively stable waves, *J. Atmos. Sci.*, *55*, 2473–2488, doi:10.1175/1520-0469(1998)055<2473:IGWBIT>2.0.CO;2.

LeLong, M.-P., and T. J. Dunkerton (1998b), Inertia-gravity wave breaking in three dimensions. 2. Convectively unstable waves, *J. Atmos. Sci.*, *55*, 2489–2501, doi:10.1175/1520-0469(1998)055<2489:IGWBIT>2.0.CO;2.

Li, F., A. Z. Liu, and G. R. Swenson (2005a), Characteristics of instabilities in the mesopause region over Maui, Hawaii, *J. Geophys. Res.*, *110*, D09S12, doi:10.1029/2004JD005097.

Li, F., A. Z. Liu, G. R. Swenson, J. H. Hecht, and W. A. Robinson (2005b), Observations of gravity wave breakdown into ripples associated with dynamical instabilities, *J. Geophys. Res.*, *110*, D09S11, doi:10.1029/2004JD004849.

Lindzen, R. S. (1981), Turbulence and stress owing to gravity wave and tidal breakdown, *J. Geophys. Res.*, *86*, 9707–9714, doi:10.1029/JC086iC10p09707.

Liu, H.-L., P. B. Hays, and R. G. Roble (1999), A numerical study of gravity wave breaking and impacts on turbulence and mean state, *J. Atmos. Sci.*, *56*, 2152–2177, doi:10.1175/1520-0469(1999)056<2152:ANSOGW>2.0.CO;2.

Liu, X., J. Xu, H. L. Liu, J. Yue, and W. Yuan (2014), Simulations of large winds and wind shears induced by gravity wave breaking in the mesosphere and lower thermosphere (MLT) region, *Ann. Geophys.*, *32*, 543–552, doi:10.5194/angeo-32-543-2014.

Lombard, P. N., and J. J. Riley (1996), Instability and breakdown of internal gravity waves. 1. Linear stability analysis, *Phys. Fluids*, *8*, 3271–3287, doi:10.1063/1.869117.

Miles, J. W. (1961), On the stability of heterogeneous shear flows, *J. Fluid Mech.*, *10*, 496–508, doi:10.1017/S0022112061000305.

She, C. Y., H. Latifi, J. R. Yu, R. J. Alvarez, R. E. Bills, and C. S. Gardner (1990), Two-frequency lidar technique for mesospheric Na temperature measurements, *Geophys. Res. Lett.*, *17*, 929–932, doi:10.1029/GL017i007p00929.

Sherman, J. P., and C.-Y. She (2006), Seasonal variation of mesopause region wind shears, convective and dynamic instabilities above Fort Collins, CO: A statistical study, *J. Atmos. Sol. Terr. Phys.*, *68*, 1061–1074, doi:10.1016/j.jastp.2006.01.011.

Sonmor, L. J., and G. P. Klaassen (1997), Toward a unified theory of gravity wave breaking, *J. Atmos. Sci.*, *54*, 2655–2680, doi:10.1175/1520-0469(1997)054<2655:TAUTOG>2.0.CO;2.

Takahashi, T., S. Nozawa, M. Tsutsumi, C. Hall, S. Suzuki, T. T. Tsuda, and R. Fujii (2014), A case study of gravity wave dissipation in the polar MLT region using sodium LIDAR and radar data, *Ann. Geophys.*, *32*(10), 1195, doi:10.5194/angeo-32-1195-2014.

Williams, B. P., M. A. White, D. A. Krueger, and C. Y. She (2002), Observation of a large amplitude wave and inversion layer leading to convective instability in the mesopause region over Fort Collins, CO (41°N, 105°W), *Geophys. Res. Lett.*, *29*(17), 1850, doi:10.1029/2001GL014514.

Xu, J., H.-L. Liu, W. Yuan, A. K. Smith, R. G. Roble, C. J. Mertens, J. M. Russell III, and M. G. Mlynczak (2007), Mesopause structure from Thermosphere, Ionosphere, Mesosphere, Energetics, and Dynamics (TIMED)/Sounding of the Atmosphere Using Broadband Emission Radiometry (SABER) observations, *J. Geophys. Res.*, *112*, D09102, doi:10.1029/2006JD007711.

Yang, G., B. Clemesha, P. Batista, and D. Simonich (2010), Seasonal variations of gravity wave activity and spectra derived from sodium temperature lidar, *J. Geophys. Res.*, *115*, D18104, doi:10.1029/2009JD012367.

Yu, J. R., and C. Y. She (1995), Climatology of a midlatitude mesopause region observed by a lidar at Fort Collins, Colorado (40.6°N, 105°W), *J. Geophys. Res.*, *100*, 7441–7452.

Zhao, Y., A. Z. Liu, and C. S. Gardner (2003), Measurements of atmospheric stability in the mesopause region at Starfire Optical Range, NM, *J. Atmos. Sol. Terr. Phys.*, *65*, 219–232, doi:10.1016/S1364-6826(02)00288-2.